



Long-chain α -olefins production over Co-MnO_x catalyst with optimized interface

Min-Li Zhu^a, Xingwu Liu^b, Yiming Niu^c, Guo-Qing Yang^a, Jun Bao^d, Yong-Hong Song^a, Yi-Fan Yan^a, Ning Du^a, Mei-Ling Shui^d, Kaiyu Zhu^b, Bingsen Zhang^c, Zhao-Tie Liu^a, Ding Ma^{b,*}, Zhong-Wen Liu^{a,*}

^a Key Laboratory of Syngas Conversion of Shaanxi Province, School of Chemistry & Chemical Engineering, Shaanxi Normal University, Xi'an 710119, China

^b Beijing National Laboratory for Molecular Sciences, College of Chemistry and Molecular Engineering, Peking University, Beijing 100871, China

^c Shenyang National Laboratory for Materials Science, Institute of Metal Research, Chinese Academy of Sciences, Shenyang 110016, China

^d Hefei National Laboratory for Physical Sciences at the Microscale, Key Laboratory of Strongly-Coupled Quantum Matter Physics of Chinese Academy of Sciences, National Synchrotron Radiation Laboratory, Key Laboratory of Surface and Interface Chemistry and Energy Catalysis of Anhui Higher Education Institutes, Department of Chemical Physics, University of Science and Technology of China, Hefei, Anhui 230026, China

ARTICLE INFO

Keywords:

Long-chain α -olefins
Fischer-Tropsch synthesis
Cobalt
Manganese oxide
Glucose

ABSTRACT

In this work, we report a carbon-mediated strategy to construct supported Co-MnO_x nano-interfacial catalyst that enables highly selective synthesis of long-chain linear α -olefins (C₅₊) via the Fischer-Tropsch (FT) reaction. The co-impregnation of glucose as the carbon precursor and metal salt aqueous solution over SiO₂ followed by pyrolysis and oxidation creates a catalyst with stable and rich Co-MnO_x nano-interfaces after reduction and under FT conditions, which are convincingly revealed from characterizations of the catalysts at different stages. The optimal catalyst is stable for over 400 h without an observably decreased CO conversion, and the highest space-time yield of C₅₊ is achieved to be 0.79 g·g_{Co}⁻¹·h⁻¹, which are mainly originated from the suppressed sintering of metallic Co and favored CO adsorption/dissociation with a reasonably inhibited H₂ co-adsorption. The simple procedure and broad availability of precursors make our developed strategy a practically important surface-engineering method capable of precisely fabricating stable nano-interfacial catalysts.

1. Introduction

The long-chain α -olefins (C₅₊) are important starting chemicals for the industrial production of synthetic lubricant, plastic, detergent, and surfactant [1]. In comparison with the petrochemical route, Fischer-Tropsch synthesis (FTS) provides an attractive alternative since it can efficiently convert the syngas (H₂ + CO) to hydrocarbons (e.g., paraffins and olefins) with largely varied carbon numbers [2–4]. To date, great efforts with significant progresses have been made in regulating the product distribution of FTS either over Fe- or Co-based catalysts [5–8]. Importantly, lower olefins (C₂–C₄) with a selectivity as high as approximately 60% can be achieved over Al₂O₃-supported iron catalysts promoted with sulfur and sodium [9], or cobalt carbide (Co₂C) nanoprisms [10]. However, selective synthesis of C₅₊ at a considerable activity level with a reasonably low CO₂ and CH₄ selectivity still remains a great challenge [11–13].

Co-based FTS catalysts are characterized by their excellent intrinsic

activity, high selectivity of long-chain hydrocarbons, and low activity for water-gas shift reaction (WGS). Because of the high chain-growth probability and hydrogenation ability, Co-based catalysts mainly produce straight-chain paraffin products [14,15]. To maximize the catalytic activity and tune the product distribution, the introduction of promoters has been identified as an effective approach by modulating the electronic structure and chemical property of cobalt besides changing supports [16,17]. Among the reported promoters, manganese oxides (MnO_x) have long been found to be effective in increasing the CO consumption rate and boosting the selectivity of lower olefins [18,19], provided that the amount, location, introducing mode of MnO_x, and the preparation method of the catalysts are optimized [20]. In this case, the structural and electronic effects between MnO_x and Co are applied to elucidate the promotional effect of MnO_x on the catalytic phenomena although the detailed promoting manner is far behind clear. Significantly, the interface between the intimately interacted Co and MnO_x is found to facilitate the dissociation & disproportionation of CO due

* Corresponding authors.

E-mail addresses: dma@pku.edu.cn (D. Ma), zwliu@snnu.edu.cn (Z.-W. Liu).

<https://doi.org/10.1016/j.apcatb.2024.123783>

Received 7 November 2023; Received in revised form 22 January 2024; Accepted 25 January 2024

Available online 28 January 2024

0926-3373/© 2024 Elsevier B.V. All rights reserved.

generally to the Lewis acidity of MnO_x [21,22], while in turn hinders the competitive adsorption of H_2 . Thus, the surface coverage ratio of adsorbed CO^* (C^*) to H^* is increased around the interfaces of Co and MnO_x .

According to the polymerization kinetics of FTS, carbon chains are prolonged via the stepwise polymerization on the surface of metal catalyst. The termination of hydrocarbon chains may involve the hydrogenation of the adsorbed hydrocarbon fragments to form *n*-paraffins or the elimination of β -hydrogen to generate α -olefins. The primary α -olefins may further participate in the secondary reactions, e.g., hydrogenation & polymerization, to produce *n*-paraffins or reinsertion into chain-growth reactions [23,24]. Thus, the distribution of specific products is determined by the surface reaction rates of the chain growth and termination. In this case, rates of the carbon-chain growth and β -H elimination are expectedly enhanced by a higher surface coverage ratio of CO^* (C^*)/ H^* , leading to a higher selectivity of long-chain olefins [25]. Following this understanding, an interfacial catalyst with plentiful Co- MnO_x nano-interfaces may promote the selectivity of long-chain olefins via increasing the surface CO^* (C^*)/ H^* ratio. Thus, different strategies have been practiced to regulate the interactions between Co and MnO_x via adjusting their spatial proximity, e.g., strong electrostatic adsorption [26], pretreatment technique [27], and support modification [28,29]. Unfortunately, the segregation and the agglomeration of MnO_x from metallic Co commonly occurs during the reduction of the catalyst and under the typical FTS conditions [30–32]. In principle, metallic Co with smaller size, creates more interfacial sites if MnO_x can be deposited in a controlled manner. Moreover, the intrinsic size effect of metallic Co on the FTS reaction is commonly observed [33,34]. Thus, the promotional effect of MnO_x on Co can be maximized if a stable Co- MnO_x nano-interface with a maximized perimeter is realized via tuning the Co size and Co- MnO_x interactions.

In this work, a carbon-mediated strategy is proposed to construct a robust nano-interfacial Co- MnO_x -(C)/ SiO_2 catalyst (Scheme 1). Specifically, given the chelating property of glucose with metal ions [35], glucose and metal precursors are first co-impregnated on SiO_2 support, and the succeeded pyrolysis (carbonization) and calcination (oxidation) lead to the oxidized Co- MnO_x -(C)/ SiO_2 catalyst. The resulting small Co_3O_4 particles are endowed with abundant surface oxygen vacancies (low-coordinated octahedral Co^{2+} ions), which facilitate dispersing and anchoring of MnO_x species. Stable and rich Co- MnO_x nano-interfaces between Co nano particles (NPs) and MnO_x islands are obtained after reduction and under FTS reaction conditions, leading to a high activity and long-term stability. The olefin selectivity of 56% with 66% C_{5+} is achieved at 210 °C over the optimal Co- MnO_x -(C)/ SiO_2 catalyst with a

CO conversion of 11.5%. Importantly, the catalyst achieves the highest space-time yield (STY) of C_{5+} , i.e., $\text{STY}_{\text{Cat.}} = 0.103 \text{ g} \cdot \text{g}_{\text{cat.}}^{-1} \cdot \text{h}^{-1}$ and $\text{STY}_{\text{Co}} = 0.79 \text{ g} \cdot \text{g}_{\text{Co}}^{-1} \cdot \text{h}^{-1}$ at 230 °C based on the mass of catalyst and metallic cobalt, respectively. The abundance and versatility of the carbon precursor and the facile impregnating process make the developed strategy a potentially important industrial method for fabricating effective and stable metal-oxide nano-interfacial catalyst.

2. Experimental section

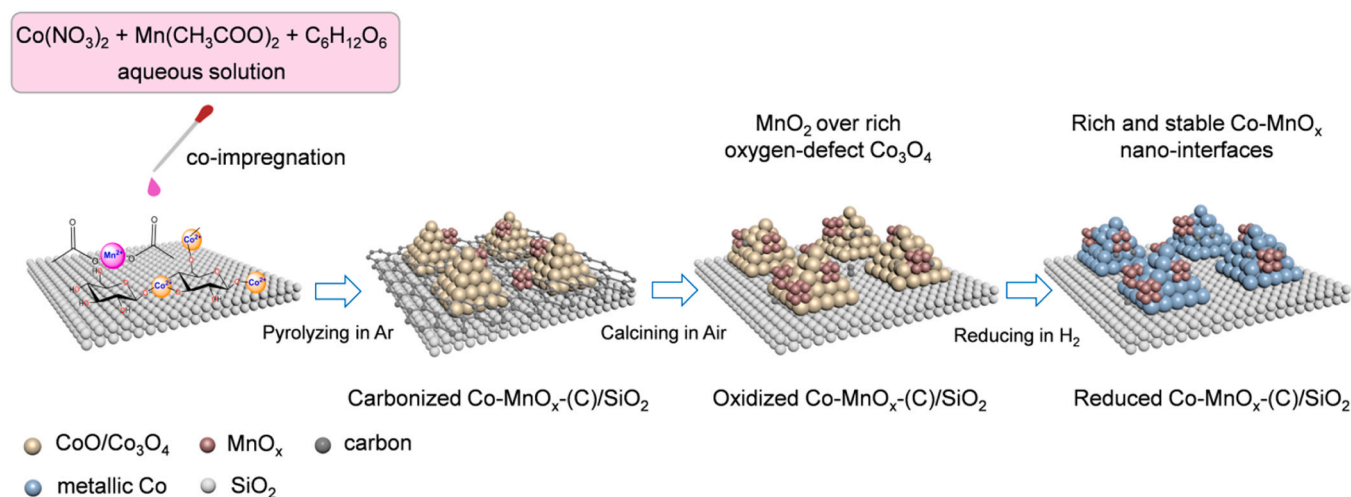
2.1. Materials

Cobalt(II) nitrate hexahydrate ($\text{Co}(\text{NO}_3)_2 \cdot 6 \text{H}_2\text{O}$, $\geq 98\%$, CAS: 10026–22–9), Manganese(II) acetate tetrahydrate ($\text{Mn}(\text{CH}_3\text{COO})_2 \cdot 4 \text{H}_2\text{O}$, $\geq 99\%$, CAS: 6156–78–1) and glucose ($\geq 99\%$, CAS: 50–99–7) were purchased from Shanghai Chemical Corp. and were used as received without any further purification. SiO_2 (Fujisilicia Q15) was purchased from Fuji Silicia Chemical Co., Ltd. and was pretreated by calcination in air at 600 °C for 3 h.

2.2. Synthesis of catalysts

The carbon-mediated strategy was accomplished in three steps, i.e., the co-impregnation of the aqueous solution of $\text{Co}(\text{NO}_3)_2$ as the cobalt precursor and glucose as the carbon source over SiO_2 followed by drying, the pyrolysis of the dried solid in an inert gas, and the subsequent oxidation in the air atmosphere. Specifically, the detailed procedure for synthesizing the Co-(C)/ SiO_2 catalyst, where C stands for the carbon-mediated strategy, was explained as follows. Firstly, by adding 2.0 g SiO_2 powder in an aqueous solution of 1.48 g $\text{Co}(\text{NO}_3)_2 \cdot 6 \text{H}_2\text{O}$ and 0.4 g glucose dissolved in 20 mL deionized water, the co-impregnation was performed at 60 °C for 90 min under a constant stirring of 400 round per minute (rpm). After removing the solvent in a rotary evaporator (100 rpm) at 60 °C, the solid was dried at 80 °C for 10 h. Subsequently, the dried sample was transferred to a tubular furnace, and the pyrolysis was conducted at 400 °C (5 °C/min) for 5 h in an Ar flow of 50 mL/min. Finally, the pyrolyzed sample was calcined in a furnace at 400 °C (5 °C/min) for 3 h in the static air atmosphere, leading to the Co-(C)/ SiO_2 catalyst.

For the synthesis of Mn-promoted catalyst of Co- MnO_x -(C)/ SiO_2 via the carbon-mediated strategy, the co-impregnation was performed by adding 2.0 g SiO_2 in an aqueous solution of 1.48 g $\text{Co}(\text{NO}_3)_2 \cdot 6 \text{H}_2\text{O}$, 0.4 g glucose, and a stoichiometric ratio of $\text{Mn}(\text{CH}_3\text{COO})_2 \cdot 4 \text{H}_2\text{O}$ dissolved in 20 mL deionized water. $\text{Mn}(\text{CH}_3\text{COO})_2 \cdot 4 \text{H}_2\text{O}$ was added to



Scheme 1. The carbon-mediated strategy for the synthesis of Co- MnO_x -(C)/ SiO_2 catalyst. The carbon-mediated strategy illustrated by using glucose as the carbon precursor for the synthesis of Co- MnO_x -(C)/ SiO_2 catalyst via the consecutive steps of co-impregnation, pyrolysis, calcination, and reduction.

achieve molar Mn/Co ratios of 0, 0.02, 0.05, 0.1, 0.2, and 0.5. If no specific value is provided, the Mn/Co molar ratio is defaulted to 0.2. After the impregnation, exactly the same procedure and parameters to those of the Co-(C)/SiO₂ catalyst were applied, leading to Co-MnO_x-(C)/SiO₂.

For a comparison purpose, the reference catalysts were synthesized without adding glucose as the carbon source during the impregnation step. Specifically, 2.0 g SiO₂ powder was added into the aqueous solution of 1.48 g Co(NO₃)₂·6 H₂O dissolved in 20 mL deionized water to implement the impregnation for synthesizing Co/SiO₂. In the same way, 2.0 g SiO₂ added in the aqueous solution of 1.48 g Co(NO₃)₂·6 H₂O and 0.25 g Mn(CH₃COO)₂·4 H₂O dissolved in 20 mL deionized water was used for the synthesis of Co-MnO_x/SiO₂. To minimize any potential effects, the steps of the impregnation, drying, pyrolysis, and calcination together with the parameters used for the carbon-mediated strategy were followed and kept the same for synthesizing Co/SiO₂ and Co-MnO_x/SiO₂ catalysts.

2.3. Material characterizations

The metal loadings were analyzed by using inductively coupled plasma-optical emission spectroscopy (ICP-OES, SPECTRO ARCOS). N₂ adsorption-desorption isotherms were tested at −196 °C using a Belsorp-Max (Bel Japan Inc.) apparatus. Prior to measurement, the samples were degassed under vacuum at 300 °C for 10 h. X-ray diffraction (XRD) patterns were obtained on a Bruker D8 Advance X-ray diffractometer with monochromatic Cu K α radiation (λ = 0.15406 nm) at 40 kV and 40 mA with a scanning speed of 0.5°·min^{−1}. The in situ XRD experiments were performed at the BL14B1 beamline (λ = 0.6887 Å, 10 keV) of the Shanghai Synchrotron Radiation Facility. The catalyst in the in situ cell was heated from 40 to 400 °C (5 °C/min) with a flow of 10% H₂/Ar at atmospheric pressure. Raman spectra were collected on a Raman spectrometer (LABRAM HR EVO, Horiba) with the excitation source laser beam of 532 nm. The wavenumber was calibrated by the peak at 520.7 cm^{−1} of a silica standard. High-resolution transmission electron microscopy (HR-TEM) images and high-angle annular dark field scanning transmission electron microscopy (HAADF-STEM) together with the elemental mapping were recorded on a TEM (FEI, TecnaiG2 F20) equipped with a Gatan Tridiem 863 P post column image filter (GIF) and a high angle energy dispersive X-ray (EDX) detector operating at 200 kV. The particle size was determined from TEM images and calculated upon the measurement of random 300 particles.

X-ray photoelectron spectroscopy (XPS) analyses were performed on an Axis Ultra spectrometer (Kratos Analytical Ltd.) using Al monochromatic X-ray source at room temperature in a high vacuum environment (approximately 5 × 10^{−9} torr). The binding energy was calibrated to the containment carbon C1s peak (284.8 eV). For the pseudo-in situ XPS study, the sample was made into small disk (6 mm diameter) and held on the sample holder. After pretreated in a flow of 10% H₂ in Ar (10 mL/min) at 400 °C for 3 h and followed by reacting in syngas (32%CO/64%H₂/4%Ar, 10 mL/min) at 220 °C for 10 h, the sample was transferred directly into an ultrahigh-vacuum chamber for XPS measurement without exposure to air. The spectra of samples after reduction or reaction were obtained under ultrahigh vacuum conditions using the monochromatic Al K α radiation. X-ray adsorption spectra of Co K-edge were obtained on the 1W1B beamline at the Beijing Synchrotron Radiation Facility (BSRF, China). The storage ring energy was 2.5 GeV with an average current of 250 mA. Energy calibration of the Co and Mn K-edge were performed using Co and Mn foil, respectively. All samples were grinded into fine powders and brushed onto adhesive tapes. Data processing was conducted by using a standard procedure of background absorption removal and normalization.

H₂ temperature programmed reduction (H₂-TPR) and O₂ titration were performed on a Micromeritics ASAP 2920 apparatus. Reduction degrees of the reduced catalysts were determined by O₂-titration at

400 °C in a flow of Ar (30 mL/min). The amount of surface metallic Co atoms was measured by the H₂ chemisorption experiment on Micromeritics ASAP 2020 C apparatus. Prior to the measurement, 100 mg of sample was reduced in pure H₂ (50 mL/min) at 400 °C for 5 h. After purging and cooling, the measurement was performed at 150 °C. The cobalt dispersion (D%) was calculated according to the equation $D = 1.179X/(W \times f)$, where X is the total H₂ uptake in $\mu\text{mol} \cdot \text{g}_{\text{cat}}^{-1}$, W is the weight percentage of cobalt, and f is the reduction degree calculated from O₂-titration. The particle size of cobalt was estimated from the H₂ uptake with the calibrated reduction degree, assuming an atomic ratio of HCo = 1 and a hemispherical crystallite geometry with a surface atomic density of 14.6 atoms/nm².

In situ diffuse reflectance infrared Fourier transform spectroscopy (DRIFTS) measurements were collected on a Bruker VERTEX70 spectrometer equipped with a MCT detector cooled by liquid N₂ and an in situ cell (Diffuse IR, PIKE Company, American) containing CaF₂ windows. For the in situ DRIFTS of CO adsorption, specifically, 50 mg of solid sample was loaded in the in situ cell and treated in a pure H₂ flow (20 mL/min) at 400 °C for 5 h under atmospheric pressure. After cooled down to room temperature, the sample was switched to a flow of Ar (20 mL/min) and the background spectrum was recorded. Then, the sample was switched to a flow of 30% CO in Ar (20 mL/min) and heated by stepwise increasing temperature from 40 to 220 °C (5 °C/min). The spectra for CO adsorption were collected every 10 °C at a resolution of 4 cm^{−1} and 64 scans. For the in situ DRIFTS experiment of CO hydrogenation, the reduced sample was flushed with Ar and the background spectrum was recorded. Afterwards, the sample was exposed to syngas (32%CO/64%H₂/4%Ar, 20 mL/min) and heated by stepwise increasing temperature from 40 to 230 °C under 0.6 MPa. The spectra were collected every 10 °C at a resolution of 4 cm^{−1} and 64 scans.

2.4. Catalytic performance test

The FTS reactions were performed in a high-pressure stainless-steel fixed-bed reactor with an inner diameter of 9 mm. Typically, 0.5 g catalyst (40–60 mesh) diluted with an equal volume of quartz sands (40–60 mesh) was loaded at the isothermal zone of the reactor. Before the FTS test, the catalyst was reduced at 400 °C and 0.1 MPa for 5 h in a pure H₂ flow of 50 mL·min^{−1}. After the reduction, the reactor was cooled to 120 °C in the H₂ flow. Then, the syngas with the volumetric composition of 32% CO, 64% H₂, and 4% Ar as the internal standard was switched, and pressurized to 1.0 MPa. The catalytic test was conducted at the reactor temperature range from 210 to 230 °C and the gas hourly space velocity (GHSV) from 2.4 to 9.6 L·g_{cat}^{−1}·h^{−1}. The tail gas out of the reactor was depressurized before entering an online gas chromatograph (GC), and the entire pipeline was kept at 300 °C to avoid the product condensation. The gases of CO, CH₄, Ar, and CO₂ in the effluent were separated using PROPAG Q and CST-TDX-01 packed columns, and analyzed on a thermal conductivity detector (TCD). Hydrocarbons (C₁–C₁₈) were separated on an HP-PONA capillary column and analyzed using a flame ionization detector (FID). For all of the FTS experiments, the carbon balance was achieved at 100 ± 10%. An illustrative scheme of the reaction system, the detailed procedure for the FTS experiments, the analyses of the products, and the calculations are given in Section 1.1 of the [Supplementary material](#).

3. Results and discussion

3.1. Catalytic performance

The nominal loading of cobalt over all of the catalysts is fixed at 13.0 wt%, and the Mn/Co molar ratio is set to be 0.2 if it is not specified, which are essentially the same as those of the measured loadings of Co and Mn (Table S1). The effect of Mn/Co molar ratio on the mass-specific activity and product distribution (Fig. S1) shows that the highest cobalt-time yield (CTY), selectivity of C₂₊ olefins (C₂₊⁺), C₅₊⁺, and olefin/

paraffin (O/P) ratios are achieved at a Mn/Co molar ratio of 0.2. When the reaction temperature is concerned (from 210 to 230 °C, Fig. S2a), the Co-MnO_x(C)/SiO₂ presents significantly higher olefin selectivity together with higher CTY and CO conversion than the other three catalysts at different reaction temperatures. In addition, STY of C₅₊ over Co-MnO_x(C)/SiO₂ at 230 °C reaches as high as 0.103 g·g_{cat}⁻¹·h⁻¹, which exceeds that over Co/SiO₂ (0.020 g·g_{cat}⁻¹·h⁻¹) by a factor of 5.2 (Fig. S2b). When the GHSV increases from 2.4 to 9.6 L·g_{cat}⁻¹·h⁻¹, the following facts are clear, i.e., the lowering of CO conversion from 75% to 11%; the simultaneous increasing of C₂₊ and C₅₊ selectivity from 22% and 15% to 50% and 36%, respectively; the dropping of C₅₊ selectivity from 66% to 30% (Fig. S3a). If the evolution of the O/P molar ratio is examined (Fig. S3b), the molar ratio of C₅₊/C₂₊ is significantly increased from 0.2 to 1.2 with increasing GHSV from 2.4 to 9.6 L·g_{cat}⁻¹·h⁻¹. These results indicate that the secondary reactions at the catalyst surface are suppressed at a higher GHSV and a lower CO conversion. Additionally, all of the counterpart catalysts show different extents of deactivation during the durability tests for a time-on-stream (TOS) of 50 h (Fig. S4a), especially for Co-(C)/SiO₂ with a fast deactivation during the initial TOS of 20 h. In contrast, Co-MnO_x(C)/SiO₂ shows the highest CO conversion of ~80% and is stable for a TOS of 400 h (Fig. S4c). Moreover, Co-MnO_x(C)/SiO₂ catalyst exhibits obviously higher olefin selectivity than other three counterparts even at a high CO conversion (Fig. S4b, Table S2).

To understand the intrinsic effect of MnO_x, FTS reactions were performed at 210 °C with a low iso-conversion level of 10 ± 1.4% via regulating GHSV. As revealed from the estimations (Section 1.2, Supplementary material), the diffusion limitations of reactants (syngas) are negligible under the tested conditions. Thus, the measured intrinsic activity can be safely discussed by correlating with the chemical and structural properties of the catalysts. From the reaction results (Fig. 1a

and Table S3), Co-MnO_x(C)/SiO₂ still shows the highest specific activity indexed by either CTY (2.6 × 10⁻⁵ mol_{CO}·g_{Co}⁻¹·s⁻¹) or turnover frequency (TOF, 0.06 s⁻¹). Moreover, clearly higher TOF and CTY over Co-MnO_x(C)/SiO₂ than those over Co-(C)/SiO₂ indicate a positive effect of MnO_x on the catalytic activity. In contrast, the introduction of MnO_x over Co-MnO_x/SiO₂ gives negligible impact on the FTS activity as revealed from the very similar CTY ((1.5 ± 0.2) × 10⁻⁵ mol_{CO}·g_{Co}⁻¹·s⁻¹) or TOF (0.03 ± 0.003 s⁻¹) with that of Co/SiO₂.

In the case of the product distribution, all of the catalysts show a similar CH₄ selectivity of 8.0 ± 1.0% and ignorable CO₂ (less than 1%), indicating the unimportant impact of MnO_x. If the olefin products are taken into account, MnO_x in the case of Co-MnO_x(C)/SiO₂ vigorously enhances the formation of olefins as indicated from the decreased selectivity of C₂₊ in the order of ~56% over Co-MnO_x(C)/SiO₂ > ~36% over Co-MnO_x/SiO₂ > ~16% over Co/SiO₂ and ~13% over Co-(C)/SiO₂. Significantly, C₃-C₁₀ olefins are dominated and C₅₊ accounts for about 66% of the total olefins over Co-MnO_x(C)/SiO₂ (Fig. 1b), leading to the much higher selectivity of C₅₊ (37%) than that over Co-(C)/SiO₂ (9%). The hydrocarbon selectivity follows ASF distributions, and the calculated chain-growth probability (denoted as α_{total}, Fig. 1c) decreases in the order of Co/SiO₂ (0.87) ≈ Co-(C)/SiO₂ (0.88) > Co-MnO_x/SiO₂ (0.82) > Co-MnO_x(C)/SiO₂ (0.76). Compared to the unprompted Co catalysts, the lower α_{total} of Co-MnO_x(C)/SiO₂ may be originated from the significant higher proportion of olefins in the products. Eventhough the magnitude contributed from the secondary reactions of α-olefin to α_{total} of FTS products is still under debate [36,37]. A decreased α_{total} over Mn-promoted catalysts was commonly obtained under the conditions that the secondary reactions of olefins were effectively suppressed [38]. Specifically, from the calculated chain-growth probability of olefins (α_{ole}) over the four tested catalysts (Fig. S5), the α_{ole}(3–8) for C₃-C₈

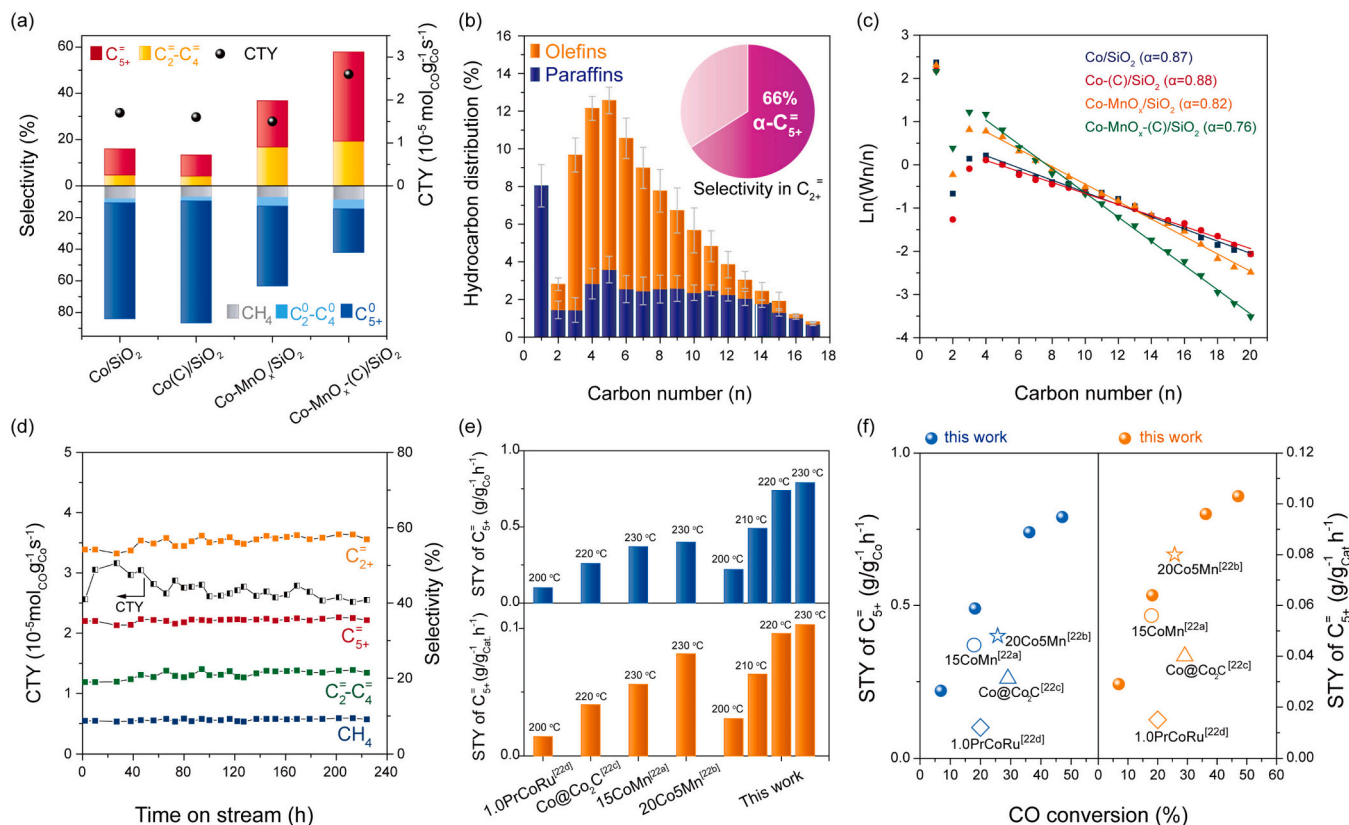


Fig. 1. Catalytic performances. (a) CTY and the product selectivity. (b) Detailed hydrocarbon distribution and selectivity of grouped olefins (inset) over Co-MnO_x(C)/SiO₂, error bounds for the selectivity of paraffins and olefins are ± 1.1% and ± 1.2%, respectively. (c) ASF plots and chain growth probabilities (α_{total}) of different catalysts. (d) Stability results over Co-MnO_x(C)/SiO₂. (e) Mass-specific productivity (STY_{cat}) and cobalt-specific productivity (STY_{Co}) of C₅₊ over Co-MnO_x(C)/SiO₂ and the published Co-based catalysts. (f) STY of C₅₊ as a function of CO conversion over Co-MnO_x(C)/SiO₂ and the published Co-based catalysts. Reaction conditions for (a-d): 0.50 g catalyst, 210 °C, 1.0 MPa, H₂/CO = 2.0, GHSV of 4.8 to 7.2 L·g_{cat}⁻¹·h⁻¹ for achieving the CO conversion at 10.0 ± 1.4%.

olefins are almost identical (0.75 ± 0.02). In contrast, the $\alpha_{\text{ole}(9-14)}$ for $\text{C}_9\text{-C}_{14}$ olefins are increased in the order of Co/SiO_2 (0.57) \approx $\text{Co-(C)}/\text{SiO}_2$ (0.56) $<$ $\text{Co-MnO}_x/\text{SiO}_2$ (0.63) $<$ $\text{Co-MnO}_x\text{-(C)}/\text{SiO}_2$ (0.70). These results clearly indicate a higher chain-growth ability of olefins on $\text{Co-MnO}_x\text{-(C)}/\text{SiO}_2$.

The superiority of $\text{Co-MnO}_x\text{-(C)}/\text{SiO}_2$ catalyst for selectively synthesizing C_5^+ is further demonstrated from the FTS results with a TOS of 200 h, and the steady-state selectivity of C_5^+ (37%), C_2^+ (56%), and CH_4 (9%) and the CTY ($2.5 \text{ mol}_{\text{CO}}/\text{g}_{\text{Co}}\cdot\text{s}^{-1}$) are kept stable without observable decrease (Fig. 1d). Thus, the long-term stability of $\text{Co-MnO}_x\text{-(C)}/\text{SiO}_2$ is reasonably expected. Moreover, in comparison with the published results for selective synthesis of long-chain olefins over Co-based FTS catalysts (Table S4) [39–42], $\text{Co-MnO}_x\text{-(C)}/\text{SiO}_2$ exhibits distinct advantages in enhancing both the catalytic activity (CTY) and the selectivity of C_5^+ while lowering the undesired by-products of CH_4 and CO_2 . To make a detailed comparison, the dependence of olefin selectivity on the CO conversion is given in Fig. S6 for $\text{Co-MnO}_x\text{-(C)}/\text{SiO}_2$, its counterpart catalysts, and those reported in references. In general, the olefin selectivity goes down with increasing CO conversion, but our $\text{Co-MnO}_x\text{-(C)}/\text{SiO}_2$ exhibits relatively higher olefin selectivity, especially C_5^+ , than that over most of the reference catalysts at the same conversion level. In addition, to quantify the productivity of C_5^+ , the STY of C_5^+ is normalized based on the weight of the loaded catalyst (the mass-specific productivity, STY_{Cat}) and the cobalt mass over the loaded catalyst (the cobalt-specific productivity, STY_{Co}), respectively. From the results given in Fig. 1e, both STY_{Cat} ($0.103 \text{ g}_{\text{C}_5^+}/\text{g}_{\text{cat}}\cdot\text{h}^{-1}$) and STY_{Co} ($0.79 \text{ g}_{\text{C}_5^+}/\text{g}_{\text{Co}}\cdot\text{h}^{-1}$) of C_5^+ over $\text{Co-MnO}_x\text{-(C)}/\text{SiO}_2$ catalyst are much higher than those reported in the references, i.e., $0.056 \text{ g}_{\text{C}_5^+}/\text{g}_{\text{cat}}\cdot\text{h}^{-1}$ and $0.37 \text{ g}_{\text{C}_5^+}/\text{g}_{\text{Co}}\cdot\text{h}^{-1}$ for $15\text{CoMn}/\text{SiO}_2$, and $0.080 \text{ g}_{\text{C}_5^+}/\text{g}_{\text{cat}}\cdot\text{h}^{-1}$ and $0.40 \text{ g}_{\text{C}_5^+}/\text{g}_{\text{Co}}\cdot\text{h}^{-1}$ for $20\text{Co5Mn}/\text{SiO}_2$ under the same reaction temperature of 230°C . The same conclusion still holds for the FTS reaction performed at a lower temperature of 220 or 200°C if $\text{Co}/\text{Co}_2\text{C}$ or $1.0\text{PrCoRu}/\text{Al}_2\text{O}_3$ is compared with our catalyst. Considering the following facts, i.e., varied FTS conditions from different research groups and the enhanced secondary reactions at a higher CO conversion, STY of C_5^+ is plotted as a function of the CO conversion. As indicated from Fig. 1f, at the same CO conversion levels, both STY_{Cat} and STY_{Co} of C_5^+ over $\text{Co-MnO}_x\text{-(C)}/\text{SiO}_2$ are still the highest among those over the available referenced catalysts. Therefore, the excellent catalytic performance and the essentially simple catalyst preparation method make $\text{Co-MnO}_x\text{-(C)}/\text{SiO}_2$ a robust and industrially important catalyst for selective synthesis C_5^+ via the FTS route.

3.2. Formation of defective Co_3O_4 NPs

Apparently, glucose plays a key role for the formation of $\text{Co-MnO}_x\text{-(C)}/\text{SiO}_2$ with the distinguished FTS performance. Thus in situ Raman was applied to probe the carbon evolution during carbonization and calcination stages of different precursors (i.e., Glu/SiO_2 , $\text{Co-Glu}/\text{SiO}_2$ and $\text{Co-Mn-Glu}/\text{SiO}_2$ by impregnating aqueous solution of glucose, glucose and Co^{2+} , and glucose, Co^{2+} and Mn^{2+} into SiO_2 , respectively) (Fig. S7). Two representative bands at around 1350 cm^{-1} (D-band) and 1600 cm^{-1} (G-band) assigning to graphitic carbon are observed over each of precursors during the carbonization process. It is noteworthy that the similar ratios of $I_{\text{D}}/I_{\text{G}}$ obtained over $\text{Co-Glu}/\text{SiO}_2$ and $\text{Co-Mn-Glu}/\text{SiO}_2$ are higher than those over Glu/SiO_2 , indicating the favorable effect of metal cations on the formation of defect-rich graphitic carbon. When these carbonaceous precursors are further calcined in air, the transformation of G-band to $D^* *$ peak occurs at above 300°C for both $\text{Co-Glu}/\text{SiO}_2$ and $\text{Co-Mn-Glu}/\text{SiO}_2$ but not for Glu/SiO_2 . This indicates that most of graphitic carbon over the precursors containing cobalt can be removed, while a tiny amount of carbon residual is still retained, which is supported by the detectable $D^* *$ peaks originated from the graphite fragments with low coordinated carbon atoms [43].

As indicated from results of the N_2 physisorption (Fig. S8 and Table S1), the calcined catalysts possess similar mesoporous textures.

The TEM images (Fig. S9) show that all of metal oxide NPs are well dispersed on the support with a mean size of $8.0 \pm 1.4 \text{ nm}$ for Co/SiO_2 , $8.2 \pm 1.5 \text{ nm}$ for $\text{Co-MnO}_x/\text{SiO}_2$, $6.7 \pm 1.1 \text{ nm}$ for $\text{Co-(C)}/\text{SiO}_2$, and $6.2 \pm 1.1 \text{ nm}$ for $\text{Co-MnO}_x\text{-(C)}/\text{SiO}_2$. The XRD patterns (Fig. 2a) of the calcined catalysts show the cubic Co_3O_4 phase (JCPDS 01–076-1802). Noticeably, the diffraction peaks observed over $\text{Co-(C)}/\text{SiO}_2$ and $\text{Co-MnO}_x\text{-(C)}/\text{SiO}_2$ are much broader than those over Co/SiO_2 and $\text{Co-MnO}_x/\text{SiO}_2$, indicating the lower crystallinity and smaller size of Co_3O_4 NPs on the carbon-mediated catalysts. Raman spectra show a set of representative active modes ($\text{A}_{1g} + 3 \text{ F}_{2g} + \text{E}_g$) attributing to the cubic Co_3O_4 structure [44] (Fig. 2b). The full width at half maximum (FWHM) of the A_{1g} bands on $\text{Co-(C)}/\text{SiO}_2$ (30 cm^{-1}) and $\text{Co-MnO}_x\text{-(C)}/\text{SiO}_2$ (50 cm^{-1}) are obviously broader than those of Co/SiO_2 (16 cm^{-1}) and $\text{Co-MnO}_x/\text{SiO}_2$ (22 cm^{-1}), suggesting an increased cation disorder and the presence of oxygen vacancies [45–47]. Moreover, it is noted that there is a red shift of A_{1g} mode from 670 cm^{-1} over $\text{Co-(C)}/\text{SiO}_2$ to 657 cm^{-1} over $\text{Co-MnO}_x\text{-(C)}/\text{SiO}_2$, which is ascribed to the increased residual stress and the lattice distortion of Co_3O_4 probably derived from the interactions between the MnO_x and the surface oxygen vacancies of Co_3O_4 .

The deconvoluted XPS spectra of Co $2p_{3/2}$ (Fig. 2c) show the clearly boosted Co^{2+} peak and stronger Co^{2+} satellites over $\text{Co-(C)}/\text{SiO}_2$ and $\text{Co-MnO}_x\text{-(C)}/\text{SiO}_2$, implying the generation of more surface Co^{2+} species over the carbon-mediated catalysts. The atomic ratios of $\text{Co}^{2+}/\text{Co}^{3+}$ for $\text{Co-(C)}/\text{SiO}_2$ and $\text{Co-MnO}_x\text{-(C)}/\text{SiO}_2$ are 7.4 and 7.9, respectively, which are significantly higher than those of Co/SiO_2 (1.8) and $\text{Co-MnO}_x/\text{SiO}_2$ (2.4) (Table S5). The typical Co_3O_4 crystal consists of the tetrahedral Co^{2+} and octahedral Co^{3+} ions, and the substantial high surface $\text{Co}^{2+}/\text{Co}^{3+}$ ratio is indicative of the presence of great amount of low-coordinated octahedral Co^{2+} ions and oxygen vacancies [48]. The lower Co chemical state of $\text{Co-(C)}/\text{SiO}_2$ and $\text{Co-MnO}_x\text{-(C)}/\text{SiO}_2$ is further verified by the Co K-edge X-ray absorption near-edge structure (XANES) spectra (Fig. S10). Moreover, the extended X-ray absorption fine structure (EXAFS) spectra (Fig. 2d) show two peaks with R space of ≈ 1.5 and $\approx 2.5 \text{ \AA}$ corresponding to the first shell Co-O and Co- Co_{long} coordinations, respectively [49]. It is obvious that $\text{Co-(C)}/\text{SiO}_2$ and $\text{Co-MnO}_x\text{-(C)}/\text{SiO}_2$ exhibit lower peak intensities of Co-O and Co- Co_{long} than those of Co/SiO_2 and $\text{Co-MnO}_x/\text{SiO}_2$, suggesting the low coordination and a low concentration of Co-O and Co- Co_{long} sites. According to the EXAFS fittings (Table S6), the Co-O coordination number (CN) of 4.0 and 4.1 for $\text{Co-(C)}/\text{SiO}_2$ and $\text{Co-MnO}_x\text{-(C)}/\text{SiO}_2$, respectively, are lower than the corresponding values of Co/SiO_2 and $\text{Co-MnO}_x/\text{SiO}_2$ (CN of 4.6 and 4.4), indicating the existence of oxygen vacancies on $\text{Co-(C)}/\text{SiO}_2$ and $\text{Co-MnO}_x\text{-(C)}/\text{SiO}_2$. The CN values of Co- Co_{long} bond for $\text{Co-(C)}/\text{SiO}_2$ (3.2) and $\text{Co-MnO}_x\text{-(C)}/\text{SiO}_2$ (4.4) are lower than those of Co/SiO_2 (5.5) and $\text{Co-MnO}_x/\text{SiO}_2$ (5.6). This indicates that Co particles on $\text{Co-(C)}/\text{SiO}_2$ and $\text{Co-MnO}_x\text{-(C)}/\text{SiO}_2$ are smaller, which are consistent with the XRD and TEM results.

3.3. Interactions between metallic Co and MnO_x

The H_2 -TPR profiles (Fig. 3a) show three H_2 -consumption peaks, which are corresponding to the reduction of Co_3O_4 to CoO (α), CoO to metallic Co (β), and cobalt species interacting with SiO_2 support (γ), respectively. The benchmark of supported MnO_x shows a small peak at around 300°C ascribing to the reduction of Mn^{4+} to Mn^{2+} [50], and it is partially overlapped with the α peak of Co_3O_4 to CoO on Mn-promoted catalyst. Significantly, the γ peak is intensified and appears at a higher temperature region over $\text{Co-(C)}/\text{SiO}_2$ and $\text{Co-MnO}_x\text{-(C)}/\text{SiO}_2$, which is originated from the small and highly dispersed Co NPs having stronger interactions with the support [51]. In addition, the β peak is broader and is shifted towards a higher temperature over the Mn-promoted catalysts relative to their counterparts without Mn, which is probably caused by the intimate interactions between CoO and MnO_x species [52]. The particle sizes and reducibility calculated from the results of H_2 -chemisorption and O_2 titration further confirm the smaller size and lower

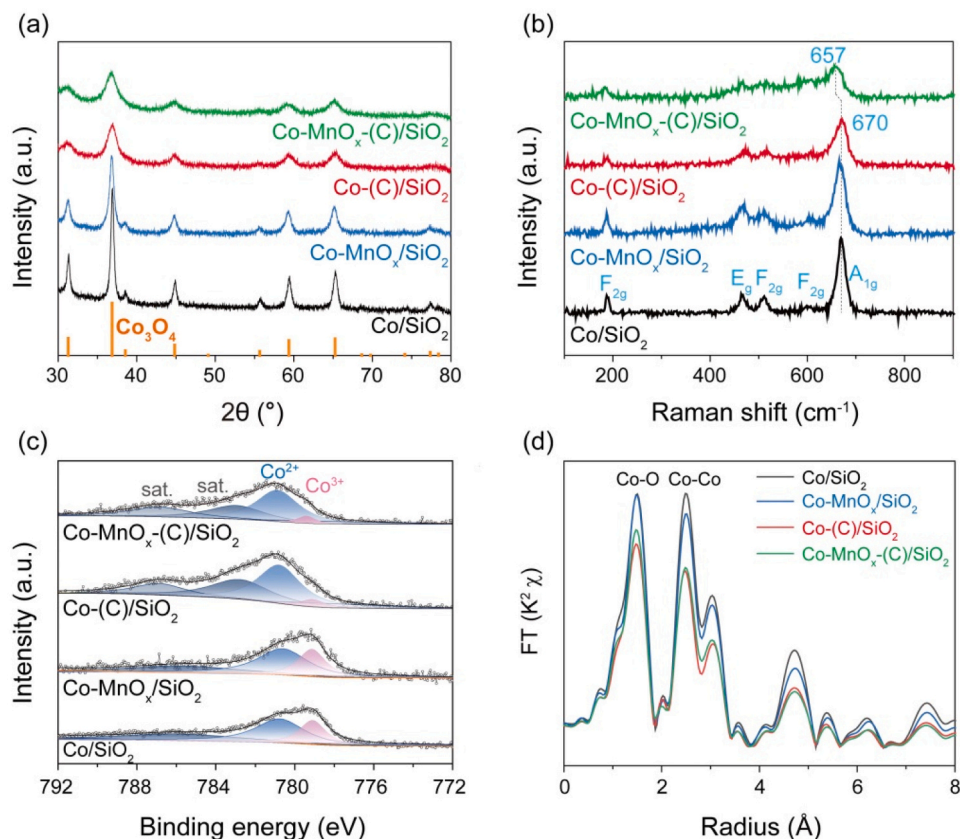


Fig. 2. Structural and chemical properties of the calcined catalysts. (a) XRD patterns, (b) Raman spectra, (c) XPS in $\text{Co } 2p_{3/2}$ regions, and (d) FT-EXAFS spectra in R space for Co K-edge.

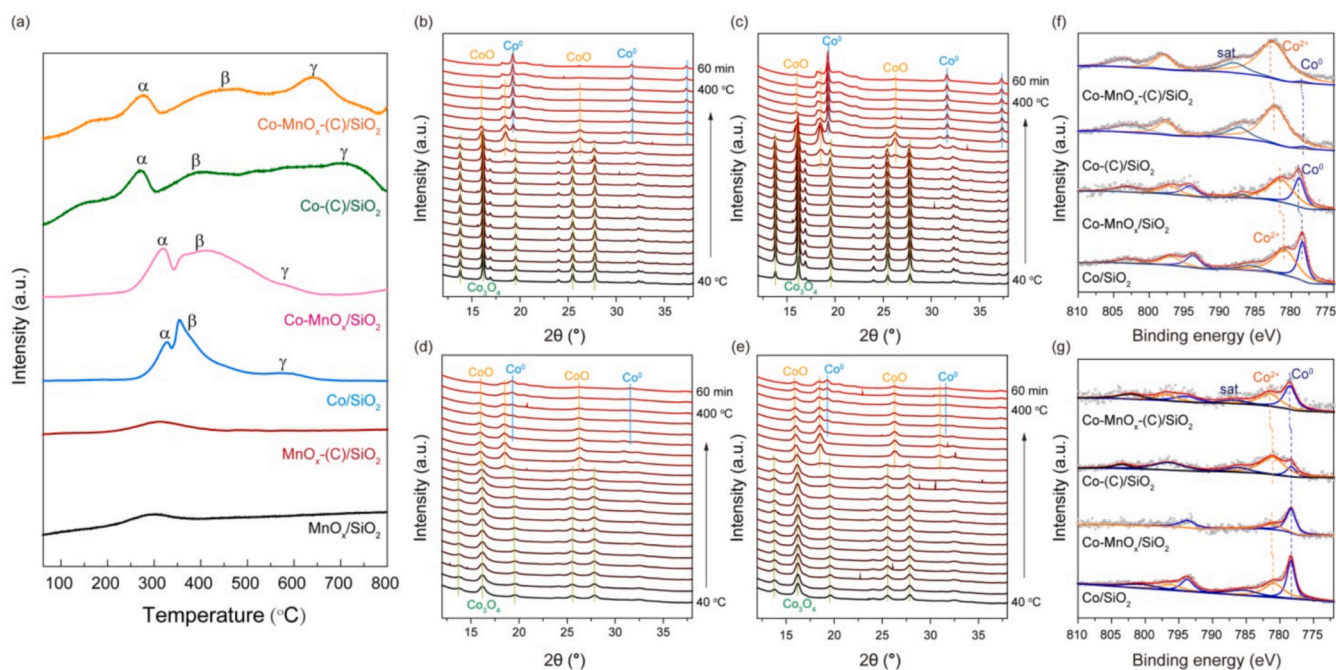


Fig. 3. Reducibility and chemical property of catalysts. (a) H_2 -TPR profiles. *In situ* XRD patterns of (b) Co/SiO_2 , (c) $\text{Co-MnO}_x\text{/SiO}_2$, (d) Co-(C)/SiO_2 , and (e) $\text{Co-MnO}_x\text{-(C)/SiO}_2$ collected from 40 to 400 $^\circ\text{C}$ in a flow of 10% H_2 /90% Ar. Pseudo-*in situ* XPS spectra in $\text{Co } 2p$ regions of the catalysts (f) after reduction and (g) after reaction.

reducibility of Co NPs on the carbon-mediated catalysts (Table S7). It is also found that the promotion of Mn decreases the catalyst reducibility but slightly influences the particle size.

In situ XRD spectra show the phase transformations from Co_3O_4 to CoO and to metallic Co (Fig. 3b-e). It is noted that the carbon-mediated catalysts show a slowness in CoO reduction, and the Mn-promotion further retards the reduction of CoO, which is more obvious on Co-MnO_x(C)/SiO₂ with the co-existence of Co⁰ and CoO under reduction at 400 °C. Given the structural properties of calcined carbon-mediated catalysts with abundant octahedral Co²⁺ ions and oxygen vacancies, it is thus proposed that the MnO_x species tend to anchor around the oxygen vacancies of octahedral Co²⁺, which reinforces the local structure and retards the CoO reduction.

The pseudo-*in situ* XPS spectra of the reduced catalysts (Fig. 3f) show that the relative contents of Co⁰ on Co/SiO₂ and Co-MnO_x/SiO₂ are higher than those on Co-(C)/SiO₂ and Co-MnO_x(C)/SiO₂, in consistent with the H₂-TPR and *in situ* XRD results. Moreover, a shift of ca. 0.4 eV to high binding energy is observed on the Mn-promoted catalysts, suggesting that the valence state of Co is more positively charged by transferring electrons to MnO_x. After FTS reaction for 10 h (Fig. 3g), the amount of Co²⁺ decreases and Co⁰ increases further (Table S5).

Meanwhile, it is stressed that the relative contents of Co⁰ on Mn-promoted catalysts are higher than those on their counterparts, which is more pronounced in the pair of Co-(C)/SiO₂ and Co-MnO_x(C)/SiO₂. Given that the surface Co⁰ species especially in small particles could be easily oxidized by water formed during FTS reaction [53,54], thus it is most likely that the interactions between Co and MnO_x in turn alleviate the oxidation of Co⁰ species. In addition, it is worth noting that such a shift in binding energy is mostly diminished on two counterparts of Co-MnO_x/SiO₂ and Co/SiO₂, which is probably due to the interface segregation of Co and MnO_x during FTS reaction [32]. In contrast, the energy shift (0.4 eV) still presents in Co-MnO_x(C)/SiO₂ as compared with Co-(C)/SiO₂, suggesting the stable interaction between Co and MnO_x.

The catalysts after reaction were further characterized to identify the active structure. XRD patterns show that metallic Co (44.2°, JCPDS 00-015-0806) is predominant on the used catalysts accompanied with weak diffractions of CoO (JCPDS 03-065-2902) (Fig. 4a). The XRD peaks over Co-(C)/SiO₂ and Co-MnO_x(C)/SiO₂ are still broader relative to those over Co/SiO₂ and Co-MnO_x/SiO₂, and no Mn species are detected. However, the Mn 2p XPS spectra and Mn K-edge XANES spectra illustrate that Mn⁴⁺ is partially reduced to Mn²⁺ on the used

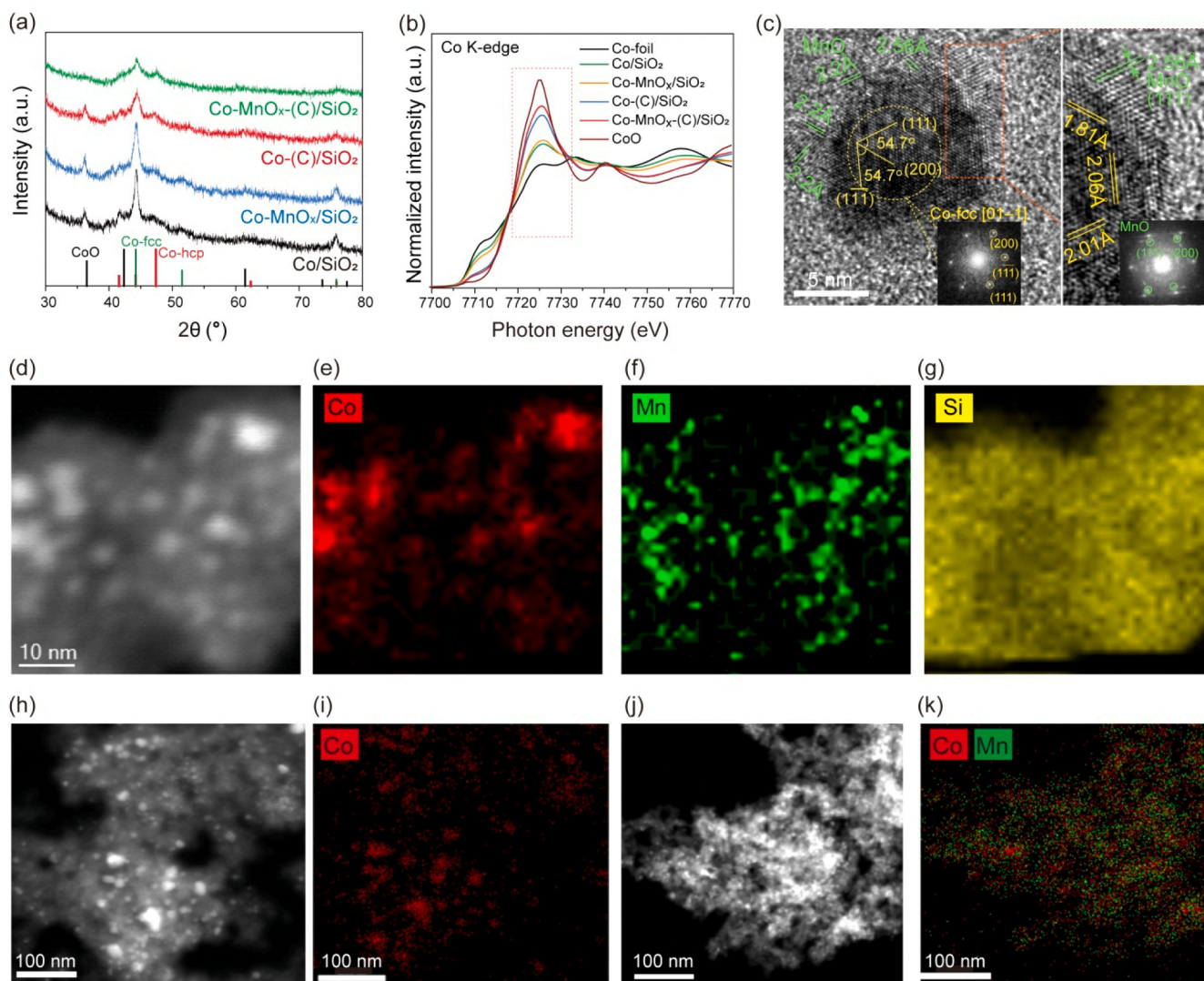


Fig. 4. Structural and chemical properties of the used catalysts. (a) XRD patterns. (b) Normalized XANES spectra at Co K-edge. (c) HR-TEM image of the used Co-MnO_x(C)/SiO₂. (d) High-resolution HAADF-STEM images on the random thin sample specimen of the used Co-MnO_x(C)/SiO₂ with the corresponding EDS elemental maps (e) for Co (red), (f) for Mn (green), and (g) for Si (yellow). HAADF-STEM images in a larger scope and the corresponding elemental mappings of the used catalysts: (h-i) Co-(C)/SiO₂ and (j-k) Co-MnO_x(C)/SiO₂. Reaction conditions: 210 °C, 1.0 MPa, H₂/CO = 2.0, TOS of 50 h.

catalysts (Fig. S11). According to the Co K-edge XANES spectra (Fig. 4b), the absorption edges of Co-(C)/SiO₂ and Co-MnO_x-(C)/SiO₂ are more close to the standard CoO, suggesting the high content of CoO. Moreover, the intensity of white line on Co-MnO_x-(C)/SiO₂ is significantly higher than that on Co-(C)/SiO₂, suggesting the pronounced electron transfer from Co to Mn. However, this is not obvious on the two counterparts of Co-MnO_x/SiO₂ and Co/SiO₂.

According to the TEM images of the used catalysts (Fig. S9), Co/SiO₂ and Co-(C)/SiO₂ exhibit obvious sintering with enlarged particle-size distributions. This phenomenon, however, is not apparent in the cases of the Mn-promoted catalysts, especially for Co-MnO_x-(C)/SiO₂, which still retains well dispersed Co NPs having a narrow size distribution similar to those of the calcined one. Moreover, the HR-STEM images of the used Co-MnO_x-(C)/SiO₂ clearly show the close spatial proximity of Co and Mn species (Fig. 4c and Fig. S12), i.e., MnO_x in the form of nanoclusters are well dispersed and attached around the metallic Co NPs, as evidenced by the lattice fringes of 2.20 Å and 2.56 Å assigning to (111) and (200) of MnO, respectively. No obvious spatial segregation occurs on the used Co-MnO_x-(C)/SiO₂ as compared to that on Co-MnO_x/SiO₂ (Fig. S12). The spatial distributions of Mn species and Co nanoparticles were further characterized by the high-magnification HAADF-STEM and corresponding X-ray energy-dispersive spectroscopy (EDS) mapping on the random thin sample specimens of the used Co-MnO_x-(C)/SiO₂ (Fig. 4d-g and Fig. S13). Clearly, Mn is intimately adjacent to Co NPs, while the phenomena of Mn-Co segregation and Mn-migration to the support surface are not observed. The HAADF-STEM image and the corresponding EDS mapping in a larger scope confirm the highly dispersed particles with homogeneous Co and Mn elements over the used Co-MnO_x-(C)/SiO₂ relative to the big particles and aggregated Co elements over the used Co-(C)/SiO₂ (Fig. 4h-k). It is thus reasonable to speculate that the stable Co-MnO_x interaction can effectively resist the sintering of Co NPs.

3.4. Insights into the formation of long-chain olefins

In situ DRIFTS spectra of CO adsorption on the reduced catalysts were collected in a flow of 30%CO/Ar with increasing the temperature (Fig. S14). At 40 °C, two bands at 2032 and 2013 cm⁻¹ ascribed to the CO linear adsorption on the top site of metallic Co (CO_{top}) are developed on the four tested catalysts, primary differences of which are higher intensities over the carbon-mediated catalysts. When the temperature is increased, the CO_{top} bands are diminished, which is most likely due to the CO desorption and/or dissociation. Considering that the carbon-mediated catalysts with small Co NPs have a great amount of step-edge and defect sites, the CO direct dissociation would occur below the CO desorption temperature [55,56]. Furthermore, at the temperature of 220 °C, a new CO_{top} peak evolves at ~2055 cm⁻¹ for Co/SiO₂ and Co-MnO_x/SiO₂. This identical CO_{top} peak (~2060 cm⁻¹) arise on Co-(C)/SiO₂ and Co-MnO_x-(C)/SiO₂ at 170 °C, and it is intensified and moves gradually to higher wavenumbers until 2072 cm⁻¹ when the temperature is increased up to 220 °C. The blue-shift of the CO_{top} peak with an increased intensity is from the improved CO coverage and the presence of co-adsorbed O or C [57,58], leading to a decreased electron back-donation from the metal site to the 2π* orbital of CO. It is thus expected that the catalysts of Co-(C)/SiO₂ and Co-MnO_x-(C)/SiO₂ have an enhanced capability for the CO adsorption and direct dissociation. Additionally, if Co-(C)/SiO₂ and Co-MnO_x-(C)/SiO₂ catalysts with comparable particle size distributions (Table S7) are compared, the CO_{top} locations and their deriving trends with increasing the temperature are basically similar during CO adsorption experiments (Fig. S14g-h). The most noticeable change of CO_{top} bands upon Mn addition is the reduced intensity, indicating a loss of active sites for the CO adsorption due to masking effect of MnO_x, which is in accordance with the characterization of H₂ chemisorption [59]. Likewise, the set of Co/SiO₂ and Co-MnO_x/SiO₂ counterparts show the same evolution phenomenon (Fig. S14e-f). Another distinguishing feature of

Mn-promoted catalysts is the adsorption band at 1589 cm⁻¹ attributed to the asymmetric *O-C-O stretching vibration [60,61], which is probably caused by the CO dissociation and disproportionation on Co-MnO_x interfaces, keeping inconsistent with the previous conclusion proposed by Johnson et al. [62].

Fig. 5a-d show *in situ* DRIFTS spectra of CO hydrogenation on the reduced catalysts with increasing temperature. The bands around 2030, 1940, and 1780 cm⁻¹ are attributed to CO adsorption on top site (CO_{top}), CO bridge-bounded (CO_{bridge}, ~1940 cm⁻¹) and CO located on threefold hollow site (CO_{hollow}, ~1780 cm⁻¹) [58], respectively. Firstly, the CO_{top} on the four catalysts is varied in intensity and frequency with increasing the temperature, and the CO_{top} frequency as a function of the temperature is shown in Fig. 5e. The CO_{top} of the Mn-promoted catalysts locate at the higher wavenumbers than those of their corresponding Co-based catalysts at temperature below 180 °C. When the temperature is increased (>180 °C), CO_{top} of Co-MnO_x/SiO₂ shifts rapidly to the lower wavenumbers similar to that of Co/SiO₂, accompanied with a quick decrease in the IR intensity. In contrast, the CO_{top} of Co-MnO_x-(C)/SiO₂ always stays about 10 cm⁻¹ wavenumbers higher than that of Co-(C)/SiO₂ throughout the whole test. Upon the introduction of syngas, the competitive adsorption between CO and H₂ occurs on the catalyst surface, leading to a decrease in the CO adsorption. Concurrently, the co-adsorbed H contributes to the electron density of the Co metal, which increases the extent of the π* back-donation to CO, resulting in a red shift of the CO_{top} peak. Given the identical locations of CO_{top} bands with 30%CO/Ar on each pair of catalysts (Fig. S14e-h), the CO_{top} peak on Co-(C)/SiO₂ displays a greater redshift than that on Co-MnO_x-(C)/SiO₂ in the presence of H₂ (Fig. 5e), suggesting a significant inhibiting effect of MnO_x on the co-adsorption of H₂ over Co-MnO_x-(C)/SiO₂ [63]. Moreover, this effect proves to be more enduring on Co-MnO_x-(C)/SiO₂ than that on Co-MnO_x/SiO₂ throughout the entire hydrogenation process. These findings support the mechanism that Mn interacting with Co particles facilitates the CO adsorption and dissociation while inhibiting the H₂ competitive adsorption, leading to an increased CO coverage over the catalyst surface. Therefore, the plentiful and stable Co-MnO_x interfaces on the Co-MnO_x-(C)/SiO₂ account for the consistent higher surface CO* (C*)/H* ratio than that on Co-(C)/SiO₂ under the FTS reaction conditions. Furthermore, Co-MnO_x-(C)/SiO₂ exhibits a substantially stronger *O-C-O peak at 1589 cm⁻¹ than Co-MnO_x/SiO₂, highlighting the stability and abundance of Co-MnO_x interfaces.

The C-H stretching regions at 3015, 2930, and 2858 cm⁻¹ corresponding to the asymmetric and symmetric stretching modes of methylene (-CH₂) group [64] are developed when temperature reaches 180 °C, suggesting the occurrence of hydrogenation and the formation of hydrocarbon products. The intensities of the major adsorbate patterns plotted as a function of temperature (Fig. 5f-i) exhibit the evolvements of the surface adsorption species and intermediates during the hydrogenation process. The intensities of the CO_{top} and *O-C-O exhibit the obvious volcano trends with increasing temperature, while the intensity of the CO_{hollow} signal hardly changes or monotonously increases with the formation of *CH_x species, suggesting that the CO_{top} and *O-C-O species are mainly responsible for the formation of hydrocarbons during the CO hydrogenation. Moreover, the significantly boosted signals of both adsorbed CO*/*O-C-O and *CH_x over Co-MnO_x-(C)/SiO₂ are indicative of the improved CO adsorption and the enhanced CO hydrogenation rate, which is in good consistent with the reaction results (Fig. 1a). Further, the synchronous products are monitored by the online MS (Fig. S15). Compared to the sole major CH₄ signal over Co/SiO₂ and Co-(C)/SiO₂, the propylene signal emerged on Mn-promoted catalysts and is greatly boosted on Co-MnO_x-(C)/SiO₂, indicating excellent ability for producing olefins.

3.5. Understanding the catalytic nature

The carbon-mediated strategy facilitates the formation of highly

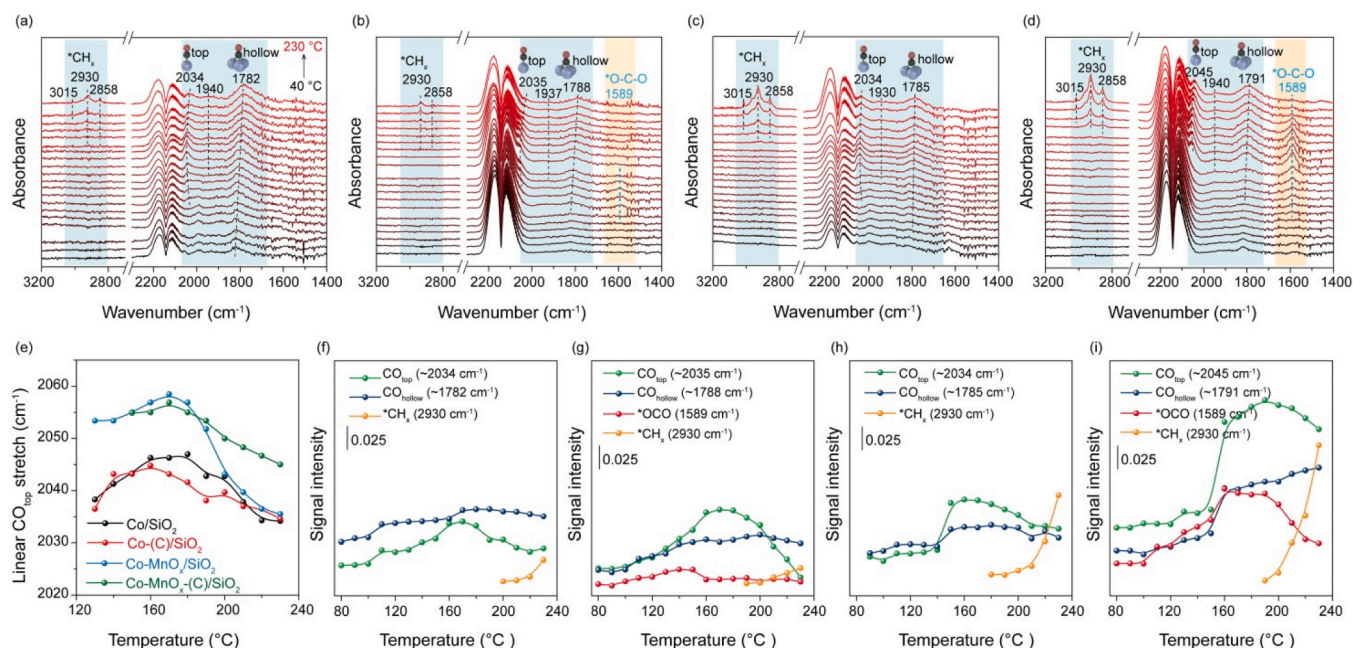


Fig. 5. Adsorbed species and reaction intermediates of FTS over the reduced catalysts. *In situ* DRIFTS collected over (a) Co/SiO₂, (b) Co-MnO_x/SiO₂, (c) Co-(C)/SiO₂, and (d) Co-MnO_x-(C)/SiO₂ from 40 to 230 °C in a flow of syngas. (e) The evolutions of the linear CO_{top} stretching frequency on temperature over the four catalysts. The changing profiles of the peak intensity for the main adsorbed species and intermediates over (f) Co/SiO₂, (g) Co-MnO_x/SiO₂, (h) Co-(C)/SiO₂, and (i) Co-MnO_x-(C)/SiO₂.

dispersed Co particles with an optimal size of ~6 nm. Moreover, the carbon-mediated procedure creates enriched octahedral Co²⁺ sites and oxygen vacancies on Co₃O₄ nanoparticles, which favor the deposition of MnO_x islands with stable and maximized Co-MnO_x perimeter. The resulting Co-MnO_x-(C)/SiO₂ catalyst after reaction still shows strong electronic interactions between Co and Mn as evidenced by the XPS peak shift (Fig. 3g). The stable Co-MnO_x nano-interfacial structure is identified by the HR-STEM and HAADF-STEM images (Fig. 4 and Fig. S12-13). The Co-MnO_x-(C)/SiO₂ catalyst exhibits an excellent activity and stability for the FTS reaction (Fig. 1). Although the surface Co⁰ sites are partially covered by MnO_x species, both CTY and TOF of Co-MnO_x-(C)/SiO₂ are still significantly higher than those of the other catalysts (Table S3). As evidenced by the *in situ* DRIFTS results of CO hydrogenation (Fig. 5), i.e., Co-MnO_x-(C)/SiO₂ displays significant high intensity of adsorbed CO* and *CH_x bands. These suggest the importance of optimized Co⁰-MnO_x nano-interfaces for enhancing the reaction activity, which is in consistent with the mechanism that the Mn²⁺ cations exposed at the edge of Co⁰-MnO_x interface may function as Lewis-acids for enhancing CO adsorption and dissociation [62]. Additionally, the dissociated O* interacting with Mn²⁺ can be removed rapidly via the formation of H₂O, resulting in the fast release of the active sites. The quick removal of *in situ* generated H₂O can also decrease the possibility for the potential oxidation of metallic Co, which is supported by the pseudo-*in situ* XPS spectra (Fig. 3g). Thus, the catalyst exhibits excellent activity and stability even at a high CO conversion of ~80% for more than 400 h (Fig. S4).

Considering that the stable and plentiful Co-MnO_x nano-interfaces over Co-MnO_x-(C)/SiO₂ can effectively decrease the availability of surface active sites involved in hydrogen adsorption and activation (H₂-chemisorption, Table S7), while facilitate CO chemisorption and dissociation, the catalyst thus possesses substantial high surface coverage ratio of CO* (C*)/H* under the FTS reaction conditions as suggested by the *in situ* DRIFTS results (Fig. 5e). Moreover, the quick hydrogenation of O* species interacting with Mn²⁺ around Co-MnO_x interface tend to drive H* migration and further decrease the H* concentration surrounding the formed hydrocarbons on Co sites. Since the surface coverages of intermediates greatly influence the elementary steps [65], the

high surface coverage ratio of CO* (C*)/H* is expected to enhance the rate of carbon-chain growth and β-H elimination while suppressing olefin hydrogenation, resulting in good selectivity of long-chain olefins as evidenced by the high signal of propylene from synchronous MS data (Fig. S15d).

In a proof-of-concept experiment (Fig. S16), the H₂/CO ratio in the gas feed was decreased from 2 to 0.5. Results show that the low H₂/CO ratio leads a two-fold increase in selectivity of olefins on both Co/SiO₂ and Co-(C)/SiO₂, suggesting an effective influence of tuning H₂/CO ratio on olefin production. In contrast, such increase in selectivity of olefins is not much pronounced on the Mn-promoted catalysts, especially for Co-MnO_x-(C)/SiO₂. This is because the Co-MnO_x nano-interfaces have already been endowed with the high surface coverage ratio of CO* (C*)/H* irrespective of the feed gas H₂/CO ratio. Moreover, the pulse experiments of propene (Fig. S17) show that the hydrogenation of olefins over Co-MnO_x-(C)/SiO₂ is less active than that over Co-(C)/SiO₂. This result agrees with the density functional theory (DFT) [66,67] that the manipulation of surface electronic property of Co by decorating with MnO_x is prone to inhibit the hydrogenation of olefins and promote olefin desorption.

4. Conclusion

In summary, the simple carbon-mediated strategy is developed to intensify the interaction between MnO_x and Co NPs via formation of defective Co₃O₄ with abundant O-deficient octahedral Co²⁺ cations and oxygen vacancies. The characterizations suggest that MnO_x species tend to anchor around the oxygen vacancies of these octahedral Co²⁺, resulting in the plentiful and stable Co-MnO_x nano-interfaces during the reduction and under FTS reaction conditions. The *in situ* spectroscopic data further demonstrates that the Co-MnO_x-(C)/SiO₂ catalyst with the stable Co-MnO_x interfaces exhibits a high surface coverage ratio of CO* (C*)/H* and thus facilitates olefins production. The resulting catalyst presents as high as of 37% selectivity of C₅⁺ and 19% selectivity towards C₂⁻-C₄⁻ at 210 °C with an improved catalytic activity, and cobalt based STY of C₅⁺ as high as of 0.79 g_{Co}⁻¹·h⁻¹ is achieved at 230 °C. Moreover, the optimal catalyst shows an excellent stability for over 400 h as a

result of the stable Co-MnO_x nano-interfaces with the suppressed sintering of Co NPs. Thus, the straightforward strategy of the carbon-mediated surface-engineering method may open up new opportunities in fabricating and tuning the nano-interfacial structure of the supported catalysts.

CRedit authorship contribution statement

Liu Zhong-Wen: Writing – review & editing, Supervision, Resources, Funding acquisition. **Zhu Kaiyu:** Data curation. **Shui Mei-Ling:** Data curation. **Du Ning:** Data curation. **Yan Yi-Fan:** Data curation. **Song Yong-Hong:** Data curation. **Bao Jun:** Resources, Data curation. **Yang Guo-Qing:** Data curation. **Niu Yiming:** Resources, Data curation. **Liu Xingwu:** Writing – original draft, Formal analysis, Data curation. **Ma Ding:** Writing – review & editing, Resources. **Zhu Min-Li:** Writing – original draft, Investigation, Formal analysis, Data curation. **Liu Zhao-Tie:** Data curation. **Zhang Bingsen:** Resources, Data curation.

Declaration of Competing Interest

The authors declare the following financial interests/personal relationships which may be considered as potential competing interests: Zhong-Wen Liu has patent #ZL2018113369370 licensed to Shaanxi Normal University. Zhong-Wen Liu has patent #ZL2018115677639 licensed to Shaanxi Normal University. If there are other authors, they declare that they have no known competing financial interests or personal relationships that could have appeared to influence the work reported in this paper.

Data availability

Data will be made available on request.

Acknowledgements

The group of Shaanxi Normal University gratefully acknowledges the financial supports of the National Natural Science Foundation of China (21808137) and the Fundamental Research Funds for the Central Universities (GK201901001).

Appendix A. Supporting information

Supplementary data associated with this article can be found in the online version at [doi:10.1016/j.apcatb.2024.123783](https://doi.org/10.1016/j.apcatb.2024.123783).

References

- J. Skupinska, Oligomerization of α -olefins to higher oligomers, *Chem. Rev.* 91 (1991) 613–648.
- J. Li, Y. He, L. Tan, P. Zhang, X. Peng, A. Oruganti, G. Yang, H. Abe, Y. Wang, N. Tsubaki, Integrated tuneable synthesis of liquid fuels via Fischer–Tropsch technology, *Nat. Catal.* 1 (2018) 787–793.
- W. Gao, Q. Zhu, D. Ma, Nanostructured catalyst for Fischer–Tropsch synthesis, *Chin. J. Chem.* 36 (2018) 798–808.
- B. Zhao, P. Zhai, P. Wang, J. Li, T. Li, M. Peng, M. Zhao, G. Hu, Y. Yang, Y.-W. Li, Q. Zhang, W. Fan, D. Ma, Direct transformation of syngas to aromatics over Na-Zn-Fe₃C₂ and hierarchical HZSM-5 tandem catalysts, *Chem* 3 (2017) 323–333.
- H.M. Torres Galvis, K.P. de Jong, Catalysts for production of lower olefins from synthesis gas: a review, *ACS Catal.* 3 (2013) 2130–2149.
- X. Peng, K. Cheng, J. Kang, B. Gu, X. Yu, Q. Zhang, Y. Wang, Impact of hydrogenolysis on the selectivity of the Fischer–Tropsch, *Synth.: Diesel fuel Prod. Mesoporous zeolite-Y-Support. Cobalt Nanopart.*, *Angew. Chem. Int. Ed.* 54 (2015) 4553–4556.
- H. Zhao, L. Jin-Xun, C. Yang, S. Yao, H.-Y. Su, Z. Gao, M. Dong, J. Wang, Y. Hou, W.-X. Li, D. Ma, Synthesis of iron-carbide nanoparticles: identification of the active phase and mechanism of Fe-based Fischer–Tropsch synthesis, *CCS Chem.* 2 (2020) 2712–2724.
- Y. Li, W. Gao, M. Peng, J. Zhang, J. Sun, Y. Xu, S. Hong, X. Liu, X. Liu, M. Wei, B. Zhang, D. Ma, Interfacial Fe₃C₂-Cu catalysts toward low-pressure syngas conversion to long-chain alcohols, *Nat. Commun.* 11 (61) (2020) 1–8.
- H.M. Torres Galvis, J.H. Bitter, C.B. Khare, M. Ruitenbeek, A.I. Dugulan, K.P. de Jong, Supported iron nanoparticles as catalysts for sustainable production of lower olefins, *Science* 335 (2012) 835–838.
- L. Zhong, F. Yu, Y. An, Y. Zhao, Y. Sun, Z. Li, T. Lin, Y. Lin, X. Qi, Y. Dai, L. Gu, J. Hu, S. Jin, Q. Shen, H. Wang, Cobalt carbide nanoprisms for direct production of lower olefins from syngas, *Nature* 538 (2016) 84–87.
- P. Zhai, Y. Li, M. Wang, J. Liu, Z. Cao, J. Zhang, Y. Xu, X. Liu, Y.-W. Li, Q. Zhu, D. Xiao, X.-D. Wen, D. Ma, Development of direct conversion of syngas to unsaturated hydrocarbons based on Fischer–Tropsch route, *Chem* 7 (2021) 3027–3051.
- T. Lin, P. Liu, K. Gong, Y. An, F. Yu, X. Wang, L. Zhong, Y. Sun, Designing silica-coated CoMn-based catalyst for Fischer–Tropsch synthesis to olefins with low CO₂ emission, *Appl. Catal. B Environ.* 299 (2021) 120683.
- K. Gong, Y. Wei, Y. Dai, T. Lin, F. Yu, Y. An, X. Wang, F. Sun, Z. Jiang, L. Zhong, Carbon-encapsulated metallic Co nanoparticles for Fischer–Tropsch to olefins with low CO₂ selectivity, *Appl. Catal. B Environ.* 316 (2022) 121700.
- Y.-H. Zhao, C. Liu, Y.-H. Song, Q.-J. Zhang, M.-L. Zhu, Z.-T. Liu, Z.-W. Liu, Direct synthesis of the reduced Co-C/SiO₂ as an efficient catalyst for Fischer–Tropsch synthesis, *Ind. Eng. Chem. Res.* 57 (2018) 1137–1145.
- Q. Cheng, Y. Tian, S. Lyu, N. Zhao, K. Ma, T. Ding, Z. Jiang, L. Wang, J. Zhang, L. Zheng, F. Gao, L. Dong, N. Tsubaki, X. Li, Confined small-sized cobalt catalysts stimulate carbon-chain growth reversibly by modifying ASF law of Fischer–Tropsch synthesis, *Nat. Commun.* 9 (2018) 3250.
- C. Hernandez Mejia, T.W. van Deelen, K.P. de Jong, Activity enhancement of cobalt catalysts by tuning metal-support interactions, *Nat. Commun.* 9 (4459) (2018) 1–8.
- Z. Gholami, Z. Tisler, V. Rubás, Recent advances in Fischer–Tropsch synthesis using cobalt-based catalysts: a review on supports, promoters, and reactors, *Catal. Rev.* 63 (2021) 512–595.
- A. Dinse, M. Aigner, M. Ulbrich, G.R. Johnson, A.T. Bell, Effects of Mn promotion on the activity and selectivity of Co/SiO₂ for Fischer–Tropsch Synthesis, *J. Catal.* 288 (2012) 104–114.
- E.Ø. Pedersen, I.-H. Svanum, E.A. Blekkan, Mn promoted Co catalysts for Fischer–Tropsch production of light olefins – An experimental and theoretical study, *J. Catal.* 361 (2018) 23–32.
- J. Xie, P.P. Paalanen, T.W. van Deelen, B.M. Weckhuysen, M.J. Louwerse, K.P. de Jong, Promoted cobalt metal catalysts suitable for the production of lower olefins from natural gas, *Nat. Commun.* 10 (2019) 167.
- G.R. Johnson, A.T. Bell, Effects of Lewis acidity of metal oxide promoters on the activity and selectivity of Co-based Fischer–Tropsch synthesis catalysts, *J. Catal.* 338 (2016) 250–264.
- R. Zhang, M. Athariboroujny, G. Collinge, V. Iablokov, K.D. Shumilov, L. Kovarik, A.N. Alexandrova, N. Kruse, J.-S. McEwen, Promoting the cleavage of C–O bonds at the interface between a metal oxide cluster and a Co(0001) support, *ACS Catal.* 10 (2020) 14722–14731.
- G.P. Van Der Laan, A.A.C.M. Beenackers, Kinetics and selectivity of the Fischer–Tropsch synthesis: a literature review, *Catal. Rev.* 41 (1999) 255–318.
- J. Cheng, T. Song, P. Hu, C.M. Lok, P. Ellis, S. French, A density functional theory study of the α -olefin selectivity in Fischer–Tropsch synthesis, *J. Catal.* 255 (2008) 20–28.
- C. Ledesma, J. Yang, E.A. Blekkan, A. Holmen, D. Chen, Carbon number dependence of reaction mechanism and kinetics in CO hydrogenation on a Co-based catalyst, *ACS Catal.* 6 (2016) 6674–6686.
- T.E. Feltes, L. Espinosa-Alonso, Ed Smit, L. D'Souza, R.J. Meyer, B.M. Weckhuysen, J.R. Regalado, Selective adsorption of manganese onto cobalt for optimized Mn/Co/TiO₂ Fischer–Tropsch catalysts, *J. Catal.* 270 (2010) 95–102.
- G.R. Johnson, A.T. Bell, Role of ZrO₂ in promoting the activity and selectivity of Co-based Fischer–Tropsch synthesis catalysts, *ACS Catal.* 6 (2015) 100–114.
- G. Bezemer, P. Radstake, U. Falke, H. Oosterbeek, H. Kuipers, A. Vandillen, K. Dejong, Investigation of promoter effects of manganese oxide on carbon nanofiber-supported cobalt catalysts for Fischer–Tropsch synthesis, *J. Catal.* 237 (2006) 152–161.
- H.G. Salazar-Contreras, A. Martínez-Hernández, A.A. Boix, G.A. Fuentes, E. Torres-García, Effect of Mn on Co/HMS-Mn and Co/SiO₂-Mn catalysts for the Fischer–Tropsch reaction, *Appl. Catal. B Environ.* 244 (2019) 414–426.
- F. Morales, D. Grandjean, F.M. de Groot, O. Stephan, B.M. Weckhuysen, Combined EXAFS and STEM-EELS study of the electronic state and location of Mn as promoter in Co-based Fischer–Tropsch catalysts, *Phys. Chem. Chem. Phys.* 7 (2005) 568–572.
- F. Sun, X. Sun, Y. Jin, R. Yang, H. Zhang, Y. Liu, F. Song, X. Li, D. Wu, T. Zhao, Z. Jiang, Microstructure evolution of a Co/MnO catalyst for Fischer–Tropsch synthesis revealed by in situ XAFS studies, *ChemCatChem* 11 (2019) 2187–2194.
- D.M. Koshy, G.R. Johnson, K.C. Bustillo, A.T. Bell, Scanning nanobeam diffraction and energy dispersive spectroscopy characterization of a model Mn-promoted Co/Al₂O₃ nanosphere catalyst for Fischer–Tropsch Synthesis, *ACS Catal.* 10 (2020) 12071–12079.
- G.L. Bezemer, J.H. Bitter, H.P.C.E. Kuipers, H. Oosterbeek, J.E. Holeywijn, X. Xu, F. Kapteijn, A.J. van Dillen, K.P. de Jong, Cobalt particle size effects in the Fischer–Tropsch reaction studied with carbon nanofiber supported catalysts, *J. Am. Chem. Soc.* 128 (2006) 3956–3964.
- Q.X. Luo, L.P. Guo, S.Y. Yao, J. Bao, Z.T. Liu, Z.W. Liu, Cobalt nanoparticles confined in carbon matrix for probing the size dependence in Fischer–Tropsch synthesis, *J. Catal.* 369 (2019) 143–156.
- L. Zhao, Y. Zhang, L.-B. Huang, X.-Z. Liu, Q.-H. Zhang, C. He, Z.-Y. Wu, L.-J. Zhang, J. Wu, W. Yang, L. Gu, J.-S. Hu, L.-J. Wan, Cascade anchoring strategy for general mass production of high-loading single-atomic metal-nitrogen catalysts, *Nat. Commun.* 10 (2019) 1278.

- [36] H. Schulz, M. Claeys, Reactions of α -olefins of different chain length added during Fischer–Tropsch synthesis on a cobalt catalyst in a slurry reactor, *Appl. Catal. A-Gen.* 186 (1999) 71–90.
- [37] S. Lögdborg, M. Lualdi, S. Järås, J.C. Walmsley, E.A. Blekkan, E. Rytter, A. Holmen, On the selectivity of cobalt-based Fischer–Tropsch catalysts: evidence for a common precursor for methane and long-chain hydrocarbons, *J. Catal.* 274 (2010) 84–98.
- [38] D. Schröder, J. Thiessen, A. Jess, J. Scholz, Influence of the formation of short-chain olefins by manganese/cobalt-catalyzed Fischer–Tropsch synthesis on the selectivity and effective reaction rate, *Catal. Sci. Technol.* 10 (2020) 475–483.
- [39] J. Zheng, J. Cai, F. Jiang, Y. Xu, X. Liu, Investigation of the highly tunable selectivity to linear α -olefins in Fischer–Tropsch synthesis over silica-supported Co and CoMn catalysts by carburization–reduction pretreatment, *Catal. Sci. Technol.* 7 (2017) 4736–4755.
- [40] Q. Lin, B. Liu, F. Jiang, X. Fang, Y. Xu, X. Liu, Assessing the formation of cobalt carbide and its catalytic performance under realistic reaction conditions and tuning product selectivity in a cobalt-based FTS reaction, *Catal. Sci. Technol.* 9 (2019) 3238–3258.
- [41] Z. Zhao, W. Lu, R. Yang, H. Zhu, W. Dong, F. Sun, Z. Jiang, Y. Lyu, T. Liu, H. Du, Y. Ding, Insight into the formation of Co@Co₂C catalysts for direct synthesis of higher alcohols and olefins from syngas, *ACS Catal.* 8 (2018) 228–241.
- [42] K. Jeske, A.C. Kizilkaya, I. López-Luque, N. Pfänder, M. Bartsch, P. Concepción, G. Prieto, Design of cobalt Fischer–Tropsch catalysts for the combined production of liquid fuels and olefin chemicals from hydrogen-rich syngas, *ACS Catal.* 11 (2021) 4784–4798.
- [43] A. Kaniyoor, S. Ramaprabhu, A. Raman, spectroscopic investigation of graphite oxide derived graphene, *AIP Adv.* 2 (2012) 032183.
- [44] J. Jiang, L. Li, Synthesis of sphere-like Co₃O₄ nanocrystals via a simple polyol route, *Mater. Lett.* 61 (2007) 4894–4896.
- [45] J.E. Spanier, R.D. Robinson, F. Zhang, S.-W. Chan, I.P. Herman, Size-dependent properties of CeO_{2–y} nanoparticles as studied by Raman scattering, *Phys. Rev. B* 64 (2001) 245407.
- [46] G. Prieto, P. Concepción, R. Murciano, A. Martínez, The impact of pre-reduction thermal history on the metal surface topology and site-catalytic activity of Fischer–Tropsch catalysts, *J. Catal.* 302 (2013) 37–48.
- [47] Z. Wang, W. Wang, L. Zhang, D. Jiang, Surface oxygen vacancies on Co₃O₄ mediated catalytic formaldehyde oxidation at room temperature, *Catal. Sci. Technol.* 6 (2016) 3845–3853.
- [48] Y. Zhang, Y. Hu, Z. Wang, T. Lin, X. Zhu, B. Luo, H. Hu, W. Xing, Z. Yan, L. Wang, Lithiation-induced vacancy engineering of Co₃O₄ with improved faradic reactivity for high-performance supercapacitor, *Adv. Funct. Mater.* 30 (2020) 2004172.
- [49] Z. Cai, Y. Bi, E. Hu, W. Liu, N. Dwarica, Y. Tian, X. Li, Y. Kuang, Y. Li, X.-Q. Yang, H. Wang, X. Sun, Single-crystalline ultrathin Co₃O₄ nanosheets with massive vacancy defects for enhanced electrocatalysis, *Adv. Energy Mater.* 8 (2018) 1701694.
- [50] L. Zhang, S. Wang, L. Lv, Y. Ding, D. Tian, S. Wang, Insights into the reactive and deactivation mechanisms of manganese oxides for ozone elimination: the roles of surface oxygen species, *Langmuir* 37 (2021) 1410–1419.
- [51] G. Prieto, A. Martínez, P. Concepción, R. Moreno-Tost, Cobalt particle size effects in Fischer–Tropsch synthesis: structural and in situ spectroscopic characterisation on reverse micelle-synthesised Co/ITQ-2 model catalysts, *J. Catal.* 266 (2009) 129–144.
- [52] O.A. Bulavchenko, T.N. Afonaseenko, A.V. Ivanchikova, V.Y. Murzin, A. Kremneva, A.A. Saraev, V.V. Kaichev, S.V. Tsybulya, In situ study of reduction of Mn_xCo_{3–x}O₄ mixed oxides: the role of manganese content, *Inorg. Chem.* 60 (2021) 16518–16528.
- [53] C. Lancelot, V.V. Ordonsky, O. Stéphan, M. Sadeqzadeh, H. Karaca, M. Lacroix, D. Curulla-Ferré, F. Luck, P. Fongarland, A. Griboval-Constant, A.Y. Khodakov, Direct evidence of surface oxidation of cobalt nanoparticles in alumina-supported catalysts for Fischer–Tropsch synthesis, *ACS Catal.* 4 (2014) 4510–4515.
- [54] P. Senecal, S.D.M. Jacques, M. Di Michiel, S.A.J. Kimber, A. Vamvakeros, Y. Odarchenko, I. Lezcano-Gonzalez, J. Paterson, E. Ferguson, A.M. Beale, Real-time scattering-contrast imaging of a supported cobalt-based catalyst body during activation and Fischer–Tropsch synthesis revealing spatial dependence of particle size and phase on catalytic properties, *ACS Catal.* 7 (2017) 2284–2293.
- [55] B. Zijlstra, R.J.P. Broos, W. Chen, H. Oosterbeek, I.A.W. Filot, E.J.M. Hensen, Coverage effects in CO dissociation on metallic cobalt nanoparticles, *ACS Catal.* 9 (2019) 7365–7372.
- [56] C.H. Wu, B. Eren, H. Bluhm, M.B. Salmeron, Ambient-pressure X-ray photoelectron spectroscopy study of cobalt foil model catalyst under CO, H₂, and their mixtures, *ACS Catal.* 7 (2017) 1150–1157.
- [57] C.D. Zeinalipour-Yazdi, R.A. van Santen, Coverage-dependent, *Adsorpt. Energy Carbon monoxide a rhodium nanocluster*, *J. Phys. Chem. C* 116 (2012) 8721–8730.
- [58] C.J. Weststrate, J. van de Loosdrecht, J.W. Niemantsverdriet, Spectroscopic insights into cobalt-catalyzed Fischer–Tropsch synthesis: a review of the carbon monoxide interaction with single crystalline surfaces of cobalt, *J. Catal.* 342 (2016) 1–16.
- [59] F. Morales, E. Desmit, F. Degroot, T. Visser, B. Weckhuysen, Effects of manganese oxide promoter on the CO and H₂ adsorption properties of titania-supported cobalt Fischer–Tropsch catalysts, *J. Catal.* 246 (2007) 91–99.
- [60] G. Prieto, M.I.S. De Mello, P. Concepción, R. Murciano, S.B.C. Pergher, An Martínez, Cobalt-catalyzed Fischer–Tropsch synthesis: chemical nature of the oxide support as a performance descriptor, *ACS Catal.* 5 (2015) 3323–3335.
- [61] S. Kattel, B. Yan, Y. Yang, J.G. Chen, P. Liu, Optimizing binding energies of key intermediates for CO₂ hydrogenation to methanol over oxide-supported copper, *J. Am. Chem. Soc.* 138 (2016) 12440–12450.
- [62] G.R. Johnson, S. Werner, A.T. Bell, An investigation into the effects of Mn promotion on the activity and selectivity of Co/SiO₂ for Fischer–Tropsch Synthesis: Evidence for enhanced CO adsorption and dissociation, *ACS Catal.* 5 (2015) 5888–5903.
- [63] M.A. Vasiliades, C.M. Kalamaras, N.S. Govender, A. Govender, A.M. Efstathiou, The effect of preparation route of commercial Co/ γ -Al₂O₃ catalyst on important Fischer–Tropsch kinetic parameters studied by SSITKA and CO-DRIFTS transient hydrogenation techniques, *J. Catal.* 379 (2019) 60–77.
- [64] C.J. Weststrate, J.W. Niemantsverdriet, CO as a promoting spectator species of C_xH_y conversions relevant for Fischer–Tropsch chain growth on cobalt: evidence from temperature-programmed reaction and reflection absorption infrared spectroscopy, *ACS Catal.* 8 (2018) 10826–10835.
- [65] A.H. Motagamwala, J.A. Dumesic, Chemical kinetics for generalized two-step reaction schemes, *J. Catal.* 404 (2021) 850–863.
- [66] Y. Qi, C. Ledesma, J. Yang, X. Duan, Y.-A. Zhu, A. Holmen, D. Chen, Adsorption energy-driven carbon number-dependent olefin to paraffin ratio in cobalt-catalyzed Fischer–Tropsch synthesis, *J. Catal.* 349 (2017) 110–117.
- [67] S. Chi, H. Huang, Y. Yu, M. Zhang, Mechanism insight into MnO for CH_x (x = 1 to 3) hydrogenation and C1–C1 coupling processes on Co(0001) surface: a DFT and kMC study, *Appl. Surf. Sci.* 586 (2022) 152840.